Nano Research

Open Access

Research Article

Diethanolamine-assisted construction of a hierarchical zeolite framework for enhanced diffusion and transformation of key intermediates in tandem catalysis

Mengting Zhang[1,§], Zhihao Chen[2,§], Jie Feng[1] ✉, Wenfeng Lang[1], Yongheng Jia[1], Peng Yuan[3], Xiaopeng Min[1], Yujia Zhang[1], Jingjing Zhao[1], Lang Wu[1], Li Han[1] ✉, and Zhikun Peng[1]

[1] *School of Ecology and Environment, Henan Institutes of Advanced Technology, State Key Laboratory of Coking Coal Resources Green Exploitation, 100 Science Road, Zhengzhou 450001, China*
[2] *Zhengzhou tobacxo research institute of CNTC, Zhengzhou 450001, China*
[3] *Henan Center for Disease Control and Prevention, Zhengzhou 450016, China*
[§] *Mengting Zhang and Zhihao Chen contributed equally to this work.*

Cite this article: *Nano Research*, **2026**, *19*, 94908673. https://doi.org/10.26599/NR.2026.94908673

ABSTRACT: Rational design of metal-acid bifunctional catalysts is crucial for steering selectivity in tandem catalysis, yet conventional metal/zeolite systems often suffer from diffusion-imposed limitations that hinder intermediate transport. Herein, we report a diethanolamine-assisted alkaline treatment (DEA-AT) strategy to reconstruct β zeolite into a hierarchical framework featuring radially aligned, exterior-connected mesoporous channels (β-DEA-AT). This architecture markedly improved the accessibility of intermediate cyclohexene to Brønsted acid sites and strengthened metal-acid cooperation in benzene hydroalkylation. As a result, Ru/β-DEA-AT catalysts delivered markedly enhanced performance, achieving a cyclohexylbenzene yield of 35.2%, benzene conversion of 62.1%, and a formation rate of 49.6 $mmol_{CHB}·g_{cat}^{-1}·h^{-1}$, surpassing both conventionally alkali-treated Ru/β-AT (30.6% conversion, 11.6% CHB yield, 31.0 $mmol_{CHB}·g_{cat}^{-1}·h^{-1}$) and pristine Ru/β catalysts (33.1% conversion, 21.6% CHB yield, 30.5 $mmol_{CHB}·g_{cat}^{-1}·h^{-1}$). Systematic investigations revealed that the DEA-induced hierarchical reconstruction facilitated the rapid migration of cyclohexene intermediates within the zeolite framework, as reflected by an increase in the apparent cyclohexene diffusion coefficient from 1.81×10^{-5} $cm^2·s^{-1}$ for $Ru/β_{100}$ to 6.42×10^{-5} $cm^2·s^{-1}$ for $Ru/β_{100}$-DEA-AT, where shortened diffusion pathways and enhanced accessibility of Brønsted acid sites promote intermediate transport and transformation. These findings establish pore-environment engineering as a generalizable strategy to regulate intermediate transformations through metal-acid synergy, providing guidance for the design of next-generation multifunctional tandem catalysts.

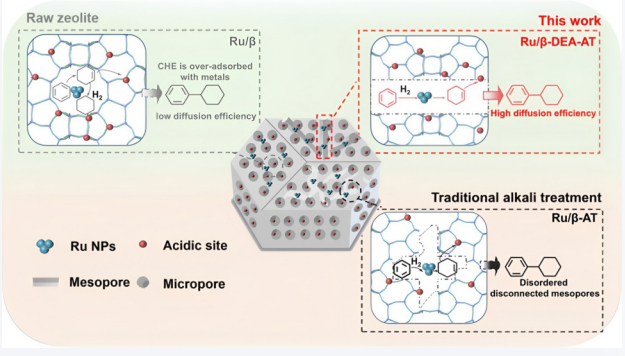

KEYWORDS: bifunctional catalysis, hierarchical zeolites, intermediate diffusion, acid site accessibility, metal-acid cooperation.

1 Introduction

Metal-acid bifunctional catalysts have long been recognized as versatile platforms for facilitating multi-step chemical transformations, especially in tandem hydroconversion (HDC) processes that converted a wide range of feedstocks into value added chemicals and fuels [1–4]. By combining metal catalyzed (de)hydrogenation [5] with acid mediated rearrangement, cleavage, or alkylation, these catalysts enabled complex transformations, such as alkane hydroisomerization, heavy fraction hydrocracking [6–9], and biomass hydrodeoxygenation within a single catalytic framework. Zeolite-supported metal catalysts (M/Zeolite) integrated metal and acid sites, enabling metal-acid coupling for tandem hydrogenation (HDC) [10–16]. Nevertheless, the intermediates generated in tandem HDC reactions were often

Received: December 19, 2025; **Revised:** March 24, 2026
Accepted: March 25, 2026

✉Address correspondence to Jie Feng, jiefeng315@zzu.edu.cn; Li Han, lihan@zzu.edu.cn

highly reactive and thermodynamically unstable. The random distribution of metal and acid sites, hindered the precise steering of intermediates, making it difficult to achieve metal-acid cooperation and limiting both selectivity and overall catalytic performance.

Significant research efforts have been directed toward balancing competing hydrogenation and acid catalyzed pathways through precise control over active site accessibility at specific reaction stages [17–21]. He et al. showed that, in a one-pot synthesis, the use of organic structure-directing agents (OSDAs) enabled fine control over Pt dispersion and its distance from Brønsted acid sites, markedly improved ethylene accessibility to the acid sites and achieved up to 98% ethylbenzene yield while enhancing resistance to sintering [22]. Ma et al. further improved reactant and branched-alkane intermediate accessibility to active sites by confining Pt clusters at both the external surface and internal channels of Hβ zeolite, resulting in substantially higher yields of short-chain alkanes and improved C_5-C_{12} selectivity [23]. In another study, Flaherty et al. demonstrated that tuning the Pt/H^+ atomic ratio in Pt-FAU could precisely modulated the formation and migration of hemiacetal intermediates, thereby dictating pathway selectivity and catalytic efficiency [24]. Collectively, these studies highlighted that optimizing metal-acid ratio and proximity could significantly strengthened metal-acid cooperation and steered selectivity toward desired products [25–28]. Nevertheless, the intrinsic diffusion constraints of key intermediates within the micropore channels, combined with their limited accessibility to specific active sites, created a fundamental mismatch between molecular transport and the metal-acid cooperativity. This intrinsic challenge underscored the need for strategies that simultaneously optimized diffusion and active-site synergy in tandem catalytic systems.

Herein, we employed a diethanolamine (DEA)-assisted alkaline treatment to reconstruct β zeolite into a hierarchical framework featuring radially aligned, exterior-connected mesoporous channels. DEA pre-impregnation directed the intrapore rearrangement, enabling the framework to retain its crystallinity and well-preserved microporosity while generating mesopores that shortened diffusion paths and exposed additional Brønsted acid sites. Such a hierarchical pore architecture markedly enhanced the accessibility of cyclohexene (CHE) to Brønsted acid sites and reinforced metal-acid cooperation in benzene hydroalkylation. Consequently, Ru/β_{100}-DEA-AT delivered substantially superior performance, affording a cyclohexylbenzene (CHB) yield of 35.2%, benzene conversion of 62.1%, and a formation rate of 49.6 $mmol_{CHB}{\cdot}g_{cat}^{-1}{\cdot}h^{-1}$, outperforming both conventionally treated Ru/β_{100}-AT (30.6% conversion, 11.6% CHB yield, 31.0 $mmol_{CHB}{\cdot}g_{cat}^{-1}{\cdot}h^{-1}$) and pristine Ru/$\beta_{100}$ catalysts (33.1% conversion, 21.6% CHB yield, 30.5 $mmol_{CHB}{\cdot}g_{cat}^{-1}{\cdot}h^{-1}$). Mechanistic investigations revealed that the DEA-induced hierarchical reconstruction facilitated the efficient migration of cyclohexene intermediates within the β-zeolite framework, as reflected by a pronounced increase in the apparent diffusion coefficient (6.42×10^{-5} $cm^2{\cdot}s^{-1}$ for Ru/β_{100}-DEA-AT versus 1.81×10^{-5} $cm^2{\cdot}s^{-1}$ for Ru/β_{100}), enabling their rapid access to neighboring Brønsted acid sites. Concurrently, the shortened diffusion pathways and enhanced acid-site accessibility promote cyclohexene transport and transformation. This hierarchical pore-engineering strategy effectively suppressed competitive deep hydrogenation and enforced an alkylation-dominated pathway in benzene hydroalkylation. These findings demonstrate that pore-environment engineering offers an effective route to steer tandem catalysis by dictating the cooperative behavior of neighboring metal and acid sites, thereby informing the design of next-generation multifunctional catalytic systems.

2 Experimental

2.1 Materials

All chemicals employed in the experiments are listed as follows: ruthenium(III) chloride (Ru 45-55%, $RuCl_3$, Aladdin), ammonium chloride (99.5%, NH_4Cl, Macklin), ammonium hydroxide (25%–30%, Innochem), sodium hydroxide (NaOH, Hushi Co., Ltd.), benzene (99.5%, C_6H_6, SCR), cyclohexene (AR, C_6H_{10}, Macklin), cyclohexyl benzene (98%, $C_{12}H_{16}$, Adamas Reagent Co., Ltd.), cyclohexane (99.7%, C_6H_{12}, Macklin), diethylamine (DEA, Macklin, ≥ 99.5 %), and β-type zeolite (molar ratios SiO_2/Al_2O_3 = 50 and 100, Hefa Catalyst Co., Ltd.).

2.2 Synthesis of Ru/β-DEA-AT catalysts (SiO_2/Al_2O_3 = 50 and 100)

Commercial β zeolites with SiO_2/Al_2O_3 molar ratios of 50 and 100 were first calcined in air at 550 °C for 6 h to eliminate residual moisture and organic impurities. Subsequently, 5 g of the calcined zeolite was suspended in 200 mL of an aqueous diethylamine (DEA) solution under vigorous stirring for 30 min. The mixture was filtered, thoroughly washed with deionized water, and dried at ambient temperature. The obtained solid was then subjected to controlled desilication in 0.2 M NaOH(aq) at 70 °C for 30 min under continuous stirring. After filtration and washing, the material was dried at 100 °C overnight and calcined at 500 °C for 2 h to remove residual organics, affording β-DEA-AT. The sample was subjected to three cycles of ion exchange using 1.0 M ammonium chloride (NH_4Cl) solution, and subsequently dried at 80 °C overnight.

For Ru loading, an aqueous solution of $RuCl_3$ (corresponding to 0.8 wt.% Ru) was added dropwise to 1 g of β-DEA-AT under vortex stirring to ensure uniform impregnation. The resulting slurry was dried at 80 °C for 12 h, followed by *in situ* reduction under 10 vol.% H_2/Ar at 400 °C for 5 h to obtain the final Ru/β-DEA-AT catalyst.

2.3 Synthesis of Ru/β-AT catalysts (SiO_2/Al_2O_3 = 50 and 100)

β zeolite (5 g, SiO_2/Al_2O_3 = 50 or 100) was treated with 0.2 M NaOH (aq) at 70 °C for 30 min under continuous stirring. The resulting solid was filtered, thoroughly washed with deionized water, and dried at 100 °C overnight to afford β-AT. Ru incorporation was achieved by dropwise impregnation of an aqueous $RuCl_3$ solution (0.8 wt.% Ru) onto 1 g of β-AT under vortex stirring to ensure uniform distribution. The sample was then dried at 80 °C for 12 h and subsequently reduced under 10 vol.% H_2/Ar at 400 °C for 5 h, yielding the Ru/β-AT catalyst. The sample was subjected to three cycles of ion exchange using 1.0 M ammonium chloride (NH_4Cl) solution, and subsequently dried at 80 °C overnight.

2.4 Synthesis of Ru/β catalysts (SiO_2/Al_2O_3 = 50 and 100)

Untreated β zeolite (SiO_2/Al_2O_3 = 50 or 100) was used directly as the support. An aqueous solution of $RuCl_3$ (0.8 wt.% Ru) was introduced dropwise onto 1 g of zeolite via incipient wetness impregnation under vortex stirring. The mixture was dried at 80 °C for 12 h and subsequently reduced under flowing 10 vol.% H_2/Ar at 400 °C for 5 h to obtain the Ru/β catalyst.

3 Results and discussion

To construct extensive mesoporosity in zeolites while minimizing the loss of microporosity and Brønsted acid sites (BAS), we developed a universal, amine assisted alkaline etching strategy. As illustrated in Fig. 1(a), this method integrated three key steps: dehydration pretreatment, DEA impregnation, and controlled desilication. The dehydration step removed the moisture in the micropores of the molecular sieve, thereby enhancing the infiltration efficiency of DEA molecules. DEA molecules selectively adsorbed within micropores, formed a protective layer that locally modulated silicon extraction during alkaline treatment. This confinement-controlled etching generated well-defined mesopores while retaining the crystallinity, intrinsic microporosity, and acid functionality of zeolite [29]. Parent β zeolite with truncated square bipyramidal morphology (Fig. 1(b)) was employed as the structural template. Upon direct alkaline treatment (β_{100}-AT, 0.2 M NaOH, 70 °C, 30 min), the zeolite retained its external geometry (Fig. 1(c)) but suffered from diminished crystallinity (Fig. 1(h)), indicative of uncontrolled framework degradation [30–32]. In contrast, DEA-assisted etching (β_{100}-DEA-AT) maintained both the morphology and diffraction integrity (Figs. 1(d) and 1(h)), highlighting the

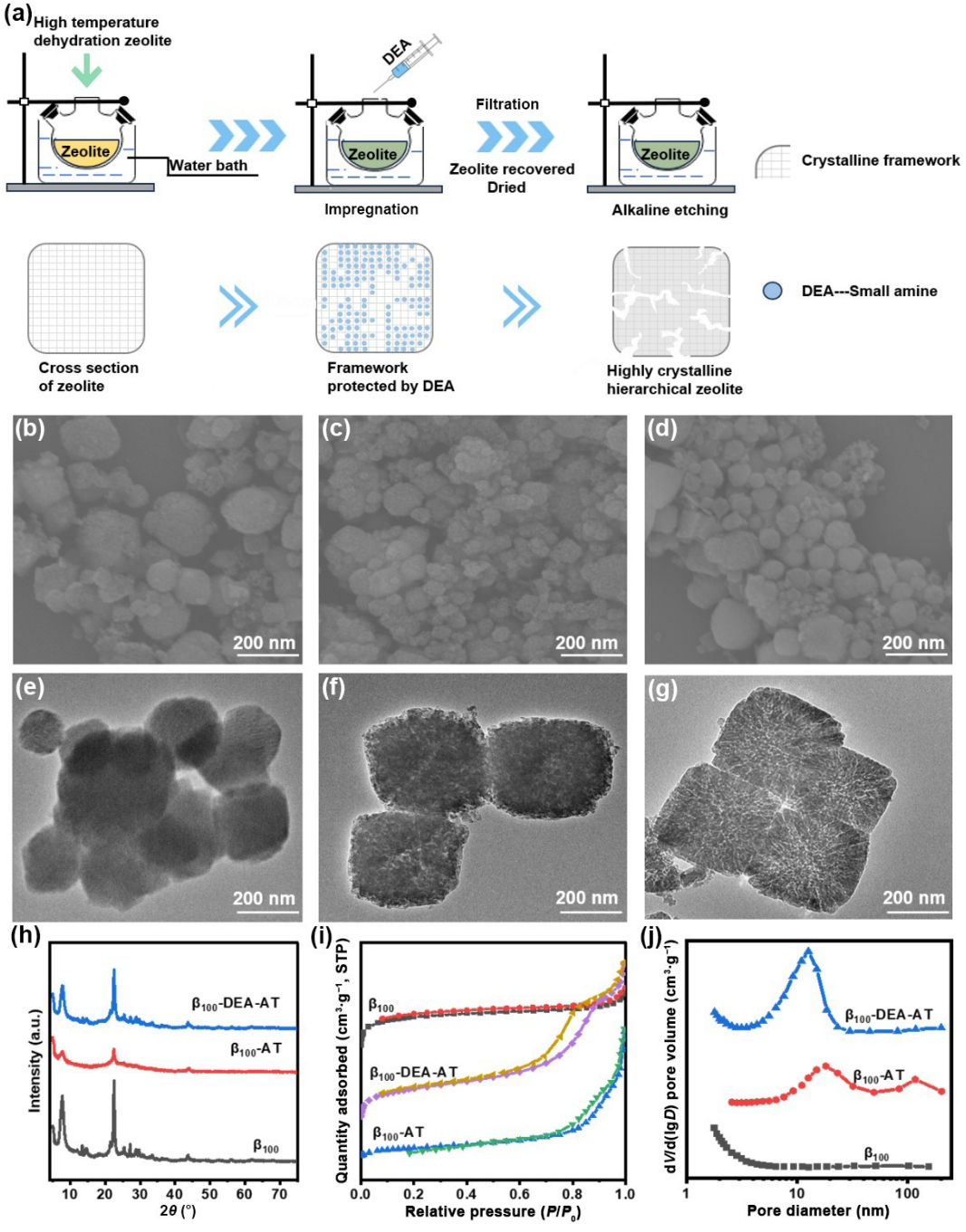

Figure 1 (a) Schematic diagram of the impregnation-desilication process. SEM images of (b) β_{100}, (c) β_{100}-AT, and (d) β_{100}-DEA-AT. TEM images of (e) β_{100}, (f) β_{100}-AT, and (g) β_{100}-DEA-AT. (h) XRD patterns of different catalysts with SiO_2/Al_2O_3 = 100. (i) N_2 adsorption–desorption isotherms, and (j) BJH pore size distribution of SiO_2/Al_2O_3 = 100 catalysts.

protective effect of DEA. TEM further revealed striking differences in pore architecture. The conventionally etched sample (β_{100}-AT, Fig. 1(f)) exhibited disordered, sponge like mesopores concentrated in the crystal core, with limited surface connectivity consistent with over-desilication and partial collapse of the internal framework. Conversely, β_{100}-DEA-AT (Fig. 1(g)) displayed a radially aligned mesoporous network extending from the crystal interior to the exterior surface. This hierarchical and open configuration enabled enhanced molecular transport, promoted rapid diffusion of reactive intermediates, and improved accessibility to acid sites. The structural characteristics described above were also observed in the β_{50} series of catalysts, demonstrating a consistent structural motif across this catalytic system (Fig. S1 in the Electronic Supplementary Material (ESM)).

Figures 1(i) and 1(j) presented the N_2 adsorption–desorption isotherms and corresponding pore size distributions for the β_{100} catalyst series. All samples exhibited pronounced nitrogen uptake at low relative pressures (P/P_0 < 0.001), indicative of preserved microporosity. Importantly, both β_{100}-AT and β_{100}-DEA-AT showed additional adsorption steps at higher relative pressures (0.6 < P/P_0 < 1.0), confirming the successful generation of mesopores *via* alkaline treatment [33]. Quantitative analysis revealed mesopore volume increased of 0.18 and 0.24 $cm^3 \cdot g^{-1}$ for β_{100}-AT and β_{100}-DEA-AT, respectively, compared to the β_{100} (Table S1 in the ESM). However, β_{100}-AT incurred a substantial 68.4% reduction in micropore volume compared to pristine β_{100}, reflecting significant framework degradation. In stark contrast, β_{100}-DEA-AT not only achieved a higher mesopore volume of 0.38 $cm^3 \cdot g^{-1}$ but also preserves 75% of the original microporosity. In the β_{50} series of catalysts, both the specific surface area and the micropore retention ratio exhibited lower values in comparison to the β_{100} series, indicating a diminished capacity for maintaining structural porosity and surface characteristics of low SiO_2/Al_2O_3(Fig. S2 and Table S1 in the ESM). These findings unambiguously demonstrated the protective effect of DEA pre-impregnation, enabling a delicate balance between mesopore formation and micropore retention.

As anticipated, the β_{100}-DEA-AT catalyst achieved a CHB selectivity of 56.6% and a yield of 35.2% at 2 h, surpassing both the conventionally alkali-treated β_{100}-AT (CHB yield of 11.6%) and the pristine β_{100} (CHB yield of 21.6%) under identical reaction conditions (Figs. 2(a)–2(c)). Notably, β_{100}-DEA-AT significantly suppressed the formation of over-hydrogenated products, achieving a CHA selectivity of 21.5% compared to 37.4% for β_{100}-AT, indicated that the DEA-assisted etching method promoted the diffusion of CHE while effectively suppressed unwanted deep hydrogenation reactions. Furthermore, a similar performance improvement was observed in the β_{50} series (Figs. 2(d)–2(f)), demonstrating the general applicability of the DEA-assisted alkaline treatment strategy. Overall, the catalytic activity followed a clear trend of Ru/β-DEA-AT > Ru/β-AT > Ru/β. Notably, β-DEA-AT exhibited superior cyclic stability, whereas β-AT, despite its higher activity relative to the pristine β zeolite, suffered severe framework degradation from conventional alkaline treatment, resulting in lower stability than both the parent β zeolite and β-DEA-AT (Fig. S5 in the ESM). These findings highlighted that the DEA-assisted etching strategy not only preserved the crystallinity and robustness of the zeolite architecture but also finely optimized metal-acid cooperation within a well-defined confined microenvironment, thereby favoring the alkylation dominated pathway over competitive deep hydrogenation.

The molar ratios of exposed metal sites (n_M) to Brønsted acid sites (n_B) were commonly employed as comparative descriptors to evaluate the metal-acid balance in the bifunctional catalysts [34–36]. As shown in Fig. 2(g), 0.8Ru/β_{100} exhibited low n_M/n_B ratio of 0.307, whereas β_{100}-DEA-AT showed increased n_M/n_B ratio of 0.372, corresponding to a R_{CHB} of 49.6 $mmol_{CHB} \cdot g_{cat}^{-1} \cdot h^{-1}$, nearly threefold higher than conventionally alkali-treated Ru/β_{100}-AT (R_{CHB} of 16.4 $mmol_{CHB} \cdot g_{cat}^{-1} \cdot h^{-1}$). During DEA-assisted alkaline treatment, DEA preferentially adsorbed within micropores, protecting the framework from excessive silica dissolution and promoting hierarchical porosity formation, with mesopore volume increasing from 0.11 to 0.35 $cm^3 \cdot g^{-1}$ and additional framework Al sites exposed. This dual effect of pore opening and enhanced acidity facilitated intermediate diffusion and optimized acid site accessibility and functional synergy. In benzene HDA, CHE intermediates were prone to deep hydrogenation on metal sites, and low n_M/n_B ratios were conventionally considered favorable for acid driven alkylation. However, the observed increase in CHB yield with n_M/n_B indicated that acid site accessibility and functional matching were the critical factors determining performance rather than stoichiometry alone. The well-balanced structure enabled rapid diffusion of CHE to accessible acid sites, suppressing secondary adsorption and over-hydrogenation on Ru. As shown in Fig. 2(h), β_{100}-DEA-AT delivered the highest CHB selectivity (56.6%), yield (35.2%), and formation rate (49.6 $mmol_{CHB} \cdot g_{cat}^{-1} \cdot h^{-1}$), with minimal CHA production. These results highlighted the pivotal role of pore environment engineering in promoting alkylation while inhibiting deep hydrogenation, and comparison with previously reported catalysts (Fig. 2(i)) underscored the exceptional performance of Ru/β_{100}-DEA-AT. The detailed comparison of the specific performance is presented in Table S4 in

Table 1 Physical and chemical property parameters of the various catalysts

Catalyst	Metal content (wt.%)[a]		SiO_2/Al_2O_3	Dispersion[b] (%)	Acidity ($\mu mol_{NH3} \cdot g_{cat}^{-1}$)[c]				Py-IR acidity ($\mu mol_{H^+} \cdot g_{cat}^{-1}$)[d]		n_M/n_B (μmol exposed Ru per μmol H^+)[e]
	Ru				Weakacid	Medium strong acid	Strong acid	Total acid	Brønsted acid	Lewis acid	
Ru/β_{50}	0.80	50	14.48	1269.3	106.3	42.6	1418.2	91.1	38.6	0.125	
Ru/β_{50}-AT	0.80	50	15.58	1074.4	88.7	36.3	1199.4	82.5	69.1	0.149	
Ru/β_{50}-DEA-AT	0.81	50	19.89	1049.1	87.1	118.1	1254.3	104.6	66.2	0.151	
Ru/β_{100}	0.80	100	15.29	971.9	—	106.9	1078.8	39.4	32.8	0.307	
Ru/β100-AT	0.81	100	9.41	1022.1	—	45.1	1067.2	27.2	39.7	0.277	
Ru/β_{100}-DEA-AT	0.80	100	21.04	1224.2	—	125.5	1349.6	69.8	44.9	0.372	

[a] Obtained from ICP-OES results. [b] Calculated from CO chemisorption. [c] Calculated from NH_3-TPD experiments. [d] Calculated from Py-IR experiments. [e] Calculated from the formula $n_M = n_{Ru} \times D_{Ru}$.

the ESM.

To elucidate the adsorption and activation behavior of key reactants and intermediates, temperature programmed desorption (TPD) and reduction (TPR) experiments were conducted. As shown in Fig. 3(a), benzene desorbed from Ru/β_{100} at ~ 162 °C, reflecting its interaction with acid sites, whereas Ru/β_{100}-DEA-AT exhibited a shift to higher temperature, indicating strengthened benzene-acid site interactions. CHE-TPD profiles (Fig. 3(b)) displayed two distinct desorption peaks: the low temperature peak corresponded to CHE on metal sites, and the high temperature peak to CHE on acidic sites [37–39]. Notably, Ru/β_{100}-DEA-AT showed a significantly intensified high temperature peak, attributable to the increased acid density and enhanced site accessibility induced by DEA-assisted desilication. This enhancement was beneficial for the protonation of CHE at acidic sites to form cyclohexyl carbon cations. In parallel, H_2-TPR analysis

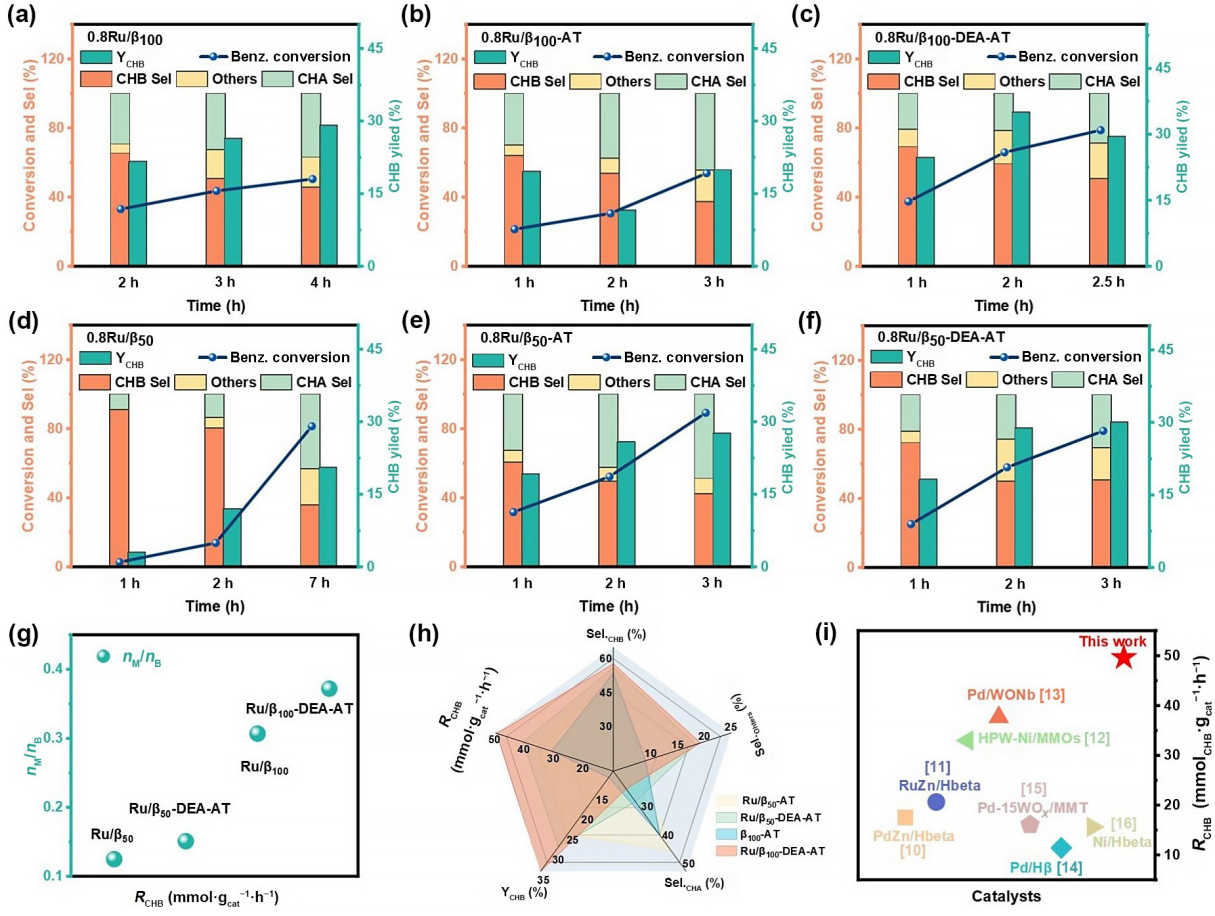

Figure 2 Product selectivity and CHB yield as a function of reaction time over (a) 0.8Ru/β_{100}, (b) 0.8Ru/β_{100}-AT, (c) 0.8Ru/β_{100}-DEA-AT, (d) 0.8Ru/β_{50}, (e) 0.8Ru/β_{50}-AT, and (f) 0.8Ru/β_{50}-DEA-AT. Reaction conditions: 0.5 g catalyst, 25 mL benzene, 4.0 MPa H_2, 200 °C, and 500 rpm. (g) The correlation between molar ratio of metal to Brønsted acid sites (n_M/n_B) and R_{CHB}. (h) Performance of different catalysts at ~ 60% benzene conversion. (i) Comparative analysis of catalytic performance in benzene HDA over reported catalytic systems.

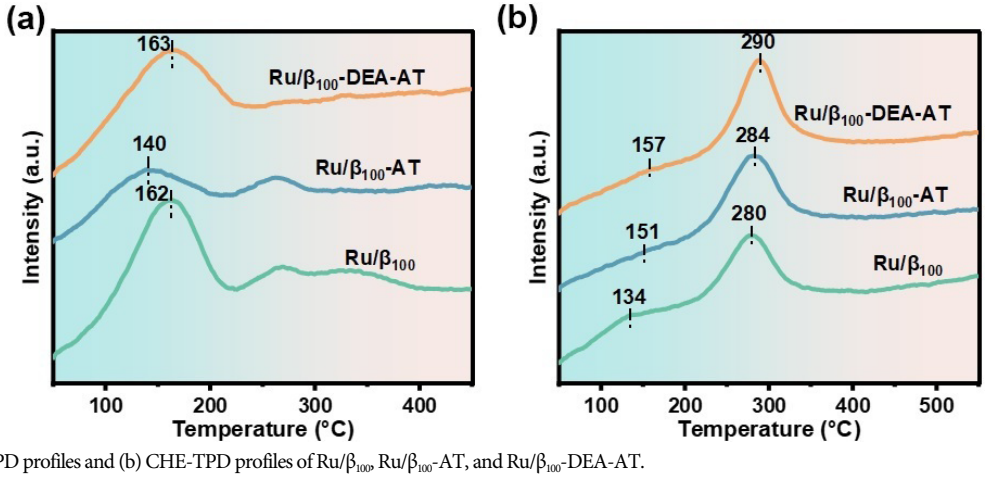

Figure 3 (a) BEN-TPD profiles and (b) CHE-TPD profiles of Ru/β_{100}, Ru/β_{100}-AT, and Ru/β_{100}-DEA-AT.

(Fig. S3(a) in the ESM) revealed a pronounced shift of the Ru reduction peak toward higher temperatures on the β_{100}-DEA-AT-supported catalyst, suggesting markedly stronger metal-support interactions. Consistently, the H_2-TPD results indicated that Ru/β_{100}-DEA-AT promoted the activation of H_2 (Fig. S3(b) in the ESM). This trend was also observed in catalysts with a low SiO_2/Al_2O_3 (Fig. S4 in the ESM).

To expound the impact of pore engineering on acid site properties, the acidity evolution of β zeolites was systematically examined via NH_3-TPD and pyridine-IR spectroscopy. Conventional alkaline treatment markedly diminished the total acidity relative to the parent zeolite, consistent with framework degradation and the concomitant loss of framework-associated Brønsted acid sites upon uncontrolled OH^- attack. In sharp contrast, the DEA-assisted strategy not only preserved but enhanced the acid site density by exposing additional micropore acid sites (Table 1). DEA molecules, pre-adsorbed within the zeolite micropores, acted as steric and chemical barriers that selectively shield framework Al from alkaline degradation. This spatial protection allowed for the controlled extraction of framework silicon, effectively lowering the SiO_2/Al_2O_3 ratio while maintaining structural integrity. On top of that, the concentration of Brønsted acid sites also increased substantially, as confirmed by the enhanced pyridine desorption signals and stronger Brønsted bands in Py-IR spectra [40] (Figs. 4(b) and 4(d)).

Figure 5(a) showed the solid-state ^{29}Si MAS NMR spectra of the β_{100} catalyst series, providing insight into the integrity of the zeolite framework [41]. The pristine β_{100} displayed characteristic Q_4 ($Si(OSi)_4$), Q_3 ($Si(OSi)_3OH$), and Q_2 ($Si(OSi)_2(OH)_2$) signals, reflecting a highly condensed silicate network. Upon conventional alkaline treatment, the pronounced attenuation of the Q_4 resonance, along with increased Q_3 and Q_2 components, signified extensive framework degradation and silanol defect formation. In contrast, the DEA-assisted sample retained a Q_4/Q_3 ratio comparable to that of the parent zeolite, unambiguously confirming that DEA pre-impregnation effectively mitigated silicon leaching and preserved the long-range framework order during desilication (Table S2 in the ESM). This structural preservation directly correlated with the retention of acid sites, as framework integrity was a prerequisite for stabilizing tetrahedrally coordinated aluminum species. Solid-state ^{27}Al MAS NMR spectra (Fig. 5(b)) supported this conclusion. β_{100}-AT exhibited a significant loss of Al(IV) (tetrahedral) signals accompanied by the emergence of extra-framework Al(VI) species, indicating framework dealumination [42, 43]. In contrast, β_{100}-DEA-AT exhibited a higher Al(IV)/Al(VI) ratio, evidencing minimal aluminum extraction and better framework stability (Table S3 in the ESM). Together, these spectroscopic analyses confirmed that DEA molecules acted as spatial modulators during alkaline treatment, selectively shielding framework sites from OH^- attack.

The adsorption-diffusion behavior within zeolite pore channels critically determined the transport of reactant molecules to active sites, thereby fundamentally governing both catalytic activity and

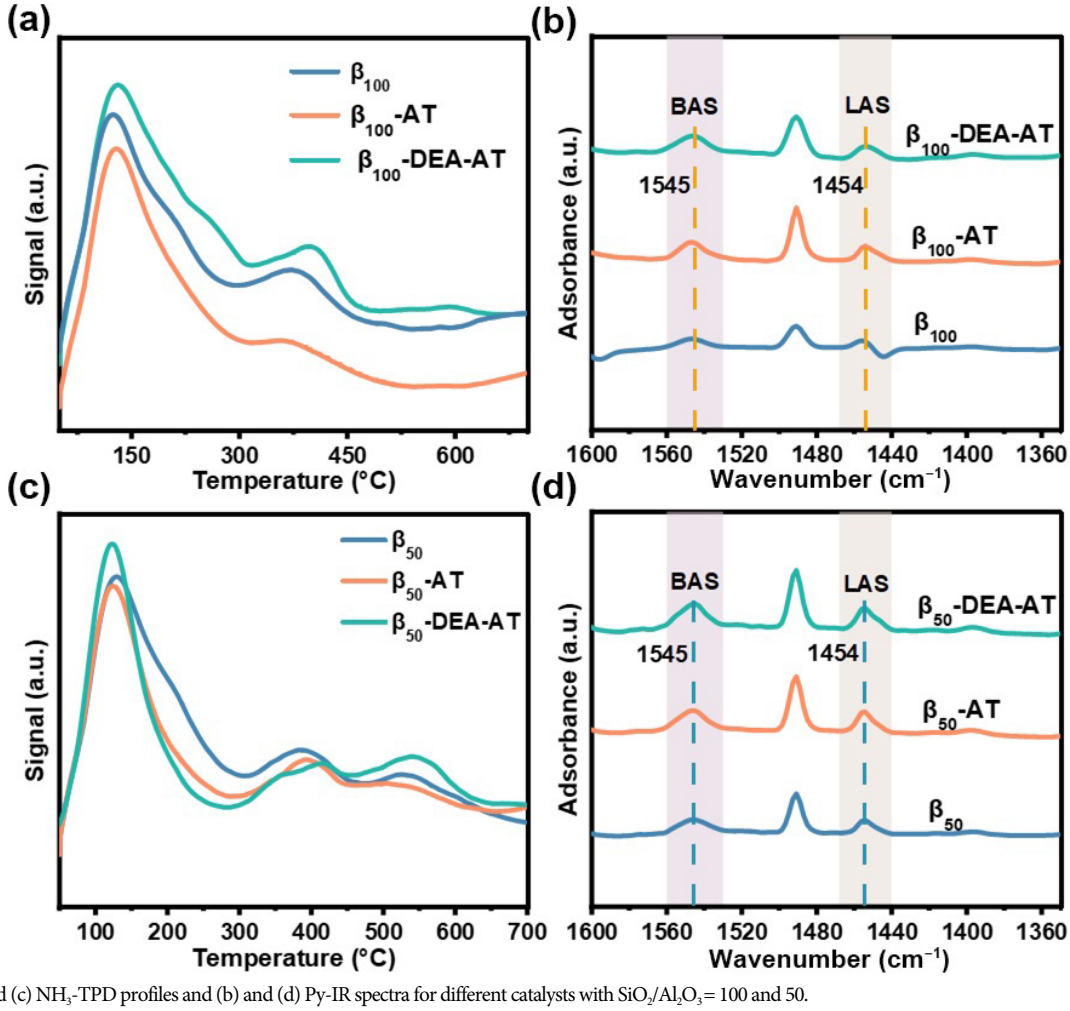

Figure 4 (a) and (c) NH_3-TPD profiles and (b) and (d) Py-IR spectra for different catalysts with SiO_2/Al_2O_3 = 100 and 50.

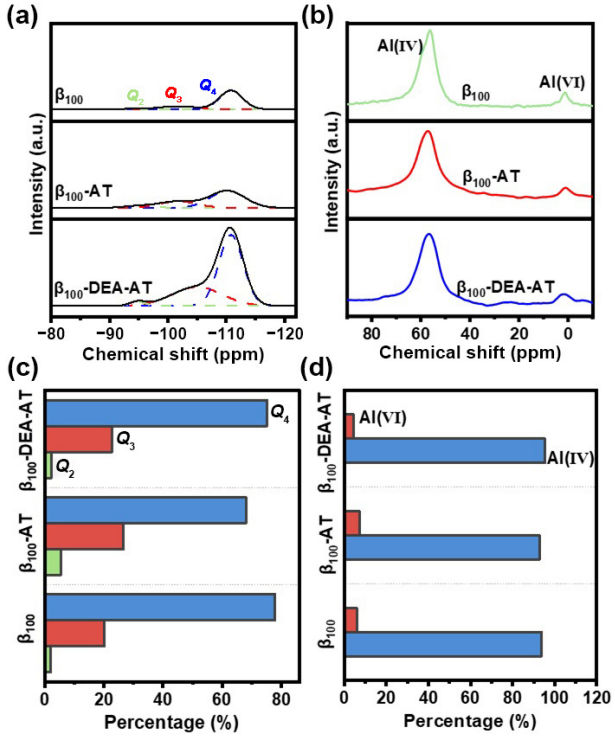

Figure 5 (a) ^{29}Si MAS NMR spectra of β_{100}, β_{100}-AT, and β_{100}-DEA-AT. (b) The spectra of ^{27}Al MAS NMR for β_{100}, β_{100}-AT and β_{100}-DEA-AT. (c) The Q_2, Q_3, and Q_4 content of β_{100}, β_{100}-AT, and β_{100}-DEA-AT. (d) The Al(IV) and Al(VI) content of β_{100}, β_{100}-AT, and β_{100}-DEA-AT.

selectivity. The impact of hierarchical porosity on diffusion behavior, as probed by CHE adsorption kinetics. During the initial adsorption period (0–100 min), β-DEA-AT exhibited a markedly steeper uptake curve compared to both the parent β zeolite and the conventionally alkali-treated β-AT sample (Figs. 6(a) and 6(c)), indicative of accelerated diffusion and shortened equilibration time. This enhanced adsorption kinetics was directly attributable to the interconnected mesopore network introduced via DEA-assisted desilication [44–46]. Quantitative diffusion analysis further supported this conclusion: the apparent diffusion coefficients for β_{50}-DEA-AT and β_{100}-DEA-AT reached 7.05×10^{-5} and 6.64×10^{-5} s^{-1}, respectively (Figs. 6(b) and 6(d)), surpassing those of both the parent and conventionally treated samples by a substantial margin. As schematically illustrated in Fig. 6(e)(II), DEA-assisted alkaline treatment generated mesopores that exposed acid sites within the micropores, enabling rapid CHE diffusion to accessible acid sites and subsequently promoting alkylation to the target CHB. In contrast, untreated β zeolite significantly hindered CHE diffusion, leading to reduced selectivity toward CHB (Fig. 6(e)(III)). The improvement arose from radially oriented mesopores that facilitated molecular transport within the zeolite crystals. Conventional alkaline treatment, by contrast, produces disordered and tortuous mesopores due to uncontrolled framework degradation, thereby limiting effective diffusion (Fig. 6(e)(I)). DEA pre-impregnation preserved the zeolite framework while generating hierarchical mesopores, enhancing molecular diffusion and exposing additional micropore acid sites [47], thereby improving Brønsted acidity and acid-metal functional synergy to enable rapid intermediate transport and support alkylation-dominated benzene HDA over Ru/β-DEA-AT.

The accessibility of Brønsted acid sites and their contribution to CHE activation were evaluated by monitoring the consumption of –OD using *in-situ* FTIR spectroscopy. (Figs. 7(a)–7(d)). Framework –OH groups were deuterated via exposure to pyridine-D5 at 300 °C, as evidenced by the disappearance of –OH stretching bands at ~ 3730 and ~ 3610 cm^{-1} and the concomitant emergence of –OD bands at ~ 2770 and ~ 2710 cm^{-1}, confirming effective substitution (Fig. S6 in the ESM). Upon introduction of CHE at ambient temperature, new absorption features appeared at 3020, 2930, and 2860 cm^{-1}, corresponding to the =C–H and –CH_2 stretching modes of the adsorbed CHE intermediate [48, 49]. Ru/β_{50} exhibited the slowest rate of –OD consumption (Fig. 7(a)). In contrast, Ru/β_{50}-DEA-AT showed a moderately faster decay, with the –OD peak intensity decreasing to 35% after 45 min (Fig. 7(b)), which could be attributed to improved mesoporosity. A significantly accelerated protonation rate was observed on Ru/β_{100} (Fig. 7(c)), compared with Ru/β_{50}. Remarkably, the –OD bands of Ru/β_{100}-DEA-AT were completely consumed within 60 min (Fig. 7(d)), highlighting the superior accessibility of Brønsted acid sites created by DEA-assisted desilication. These findings demonstrated that DEA treatment not only generated a hierarchically mesoporous network but also preserved and exposed micropore Brønsted acid sites, thereby synergistically enhancing the activation of carbocationic intermediates in benzene hydroalkylation. The effect was particularly evident in β zeolites with higher SiO_2/Al_2O_3 ratios, where maintaining framework stability was crucial. Quantitative analysis of the –OD peak evolution established the following trend in CHE protonation efficiency (Fig. 7(e)): Ru/β_{100}-DEA-AT > Ru/β_{50}-DEA-AT > Ru/β_{100} > Ru/β_{50}. This order correlated well with catalytic performance (Fig. 7(f)), reinforcing that the spatial accessibility of Brønsted acid sites was a decisive factor in achieving high CHB selectivity and yield.

4 Conclusions

In summary, we developed a diethanolamine-assisted alkaline treatment (DEA-AT) strategy to reconstruct β zeolite into a hierarchical framework with radially aligned, exterior-connected mesoporous channels (β-DEA-AT). This architecture preserved the crystalline framework and intrinsic microporosity while shortening diffusion pathways and exposing abundant Brønsted acid sites, thereby markedly enhancing cyclohexene transport and transformation and enabling more efficient metal–acid synergy. As a result, Ru/β-DEA-AT exhibited substantially improved benzene hydroalkylation performance, achieved a CHB yield of 35.2%, benzene conversion of 62.1%, and a formation rate of 49.6 $mmol_{CHB} \cdot g_{cat}^{-1} \cdot h^{-1}$, surpassed both conventionally alkali-treated Ru/β-AT (30.6% conversion, 11.6% CHB yield 31.0 $mmol_{CHB} \cdot g_{cat}^{-1} \cdot h^{-1}$) and pristine Ru/β catalysts (33.1% conversion, 21.6% CHB yield 30.5 $mmol_{CHB} \cdot g_{cat}^{-1} \cdot h^{-1}$). Mechanistic investigations revealed that the DEA-induced hierarchical reconstruction facilitated the efficient migration of cyclohexene intermediates within the β-zeolite framework, as reflected by a pronounced increase in the apparent diffusion coefficient (6.42×10^{-5} $cm^2 \cdot s^{-1}$ for Ru/β_{100}-DEA-AT versus 1.81×10^{-5} $cm^2 \cdot s^{-1}$ for Ru/β_{100}), enabling their rapid access to neighboring Brønsted acid sites. This hierarchical pore-engineering strategy enforced an alkylation-dominated pathway by suppressing competitive cyclohexene hydrogenation. The work highlights the critical role of pore environment engineering, providing a generalizable strategy for designing multifunctional tandem catalysts with optimized intermediate transformations.

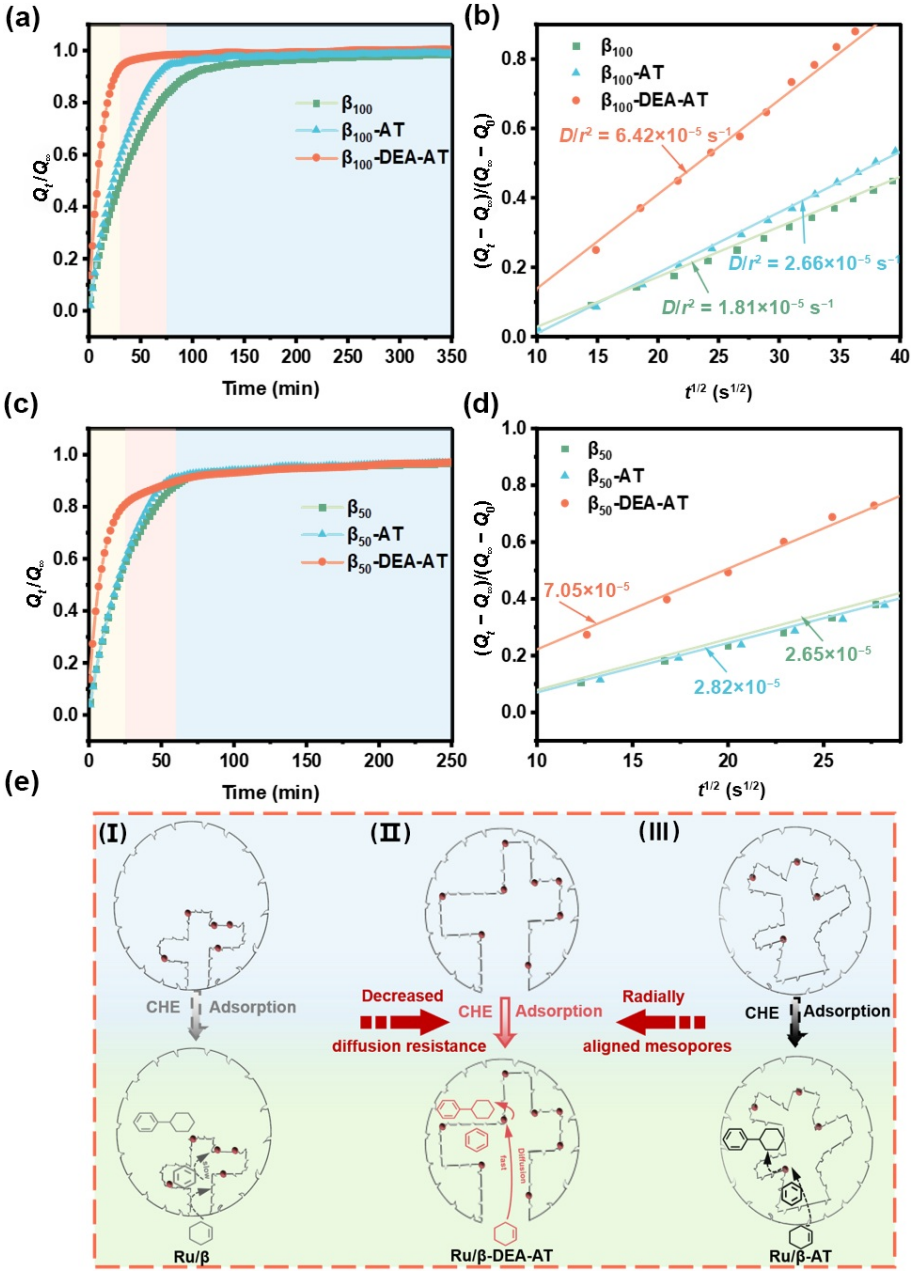

Figure 6 (a) CHE absorption curves of β_{100}, β_{100}-AT, and β_{100}-DEA-AT. (b) Normalized amount of adsorption profiles in a short time. (c) CHE absorption curves of β_{50}, β_{50}-AT, and β_{50}-DEA-AT. (d) Normalized amount of adsorption profiles in a short time domain. (e) Schematic illustration of the rapid diffusion of CHE within the β-DEA-AT catalyst.

Electronic Supplementary Material: Supplementary material is available in the online version of this article at https://doi.org/10.26599/NR.2026.94908673.

Acknowledgements

All data needed to support the conclusions in the paper are presented in the manuscript and the Electronic Supplementary Material. Additional data related to this paper may be requested from the corresponding author upon request.

Acknowledgements

This work was financially supported by the National Natural Science Foundation of China (No. 22278380), the National Key Research and Development Program (No. 2022YFE0208300), the Excellent Youth of Henan Province (No. 242300421122), and the China Postdoctoral Science Foundation (No. 2025M771261).

Declaration of competing interest

The authors declare that they have no known competing financial interests or personal relationships that could have appeared to influence the work reported in this paper.

Author contribution statement

M. T. Z.: Investigation, validation, formal analysis, writing – review

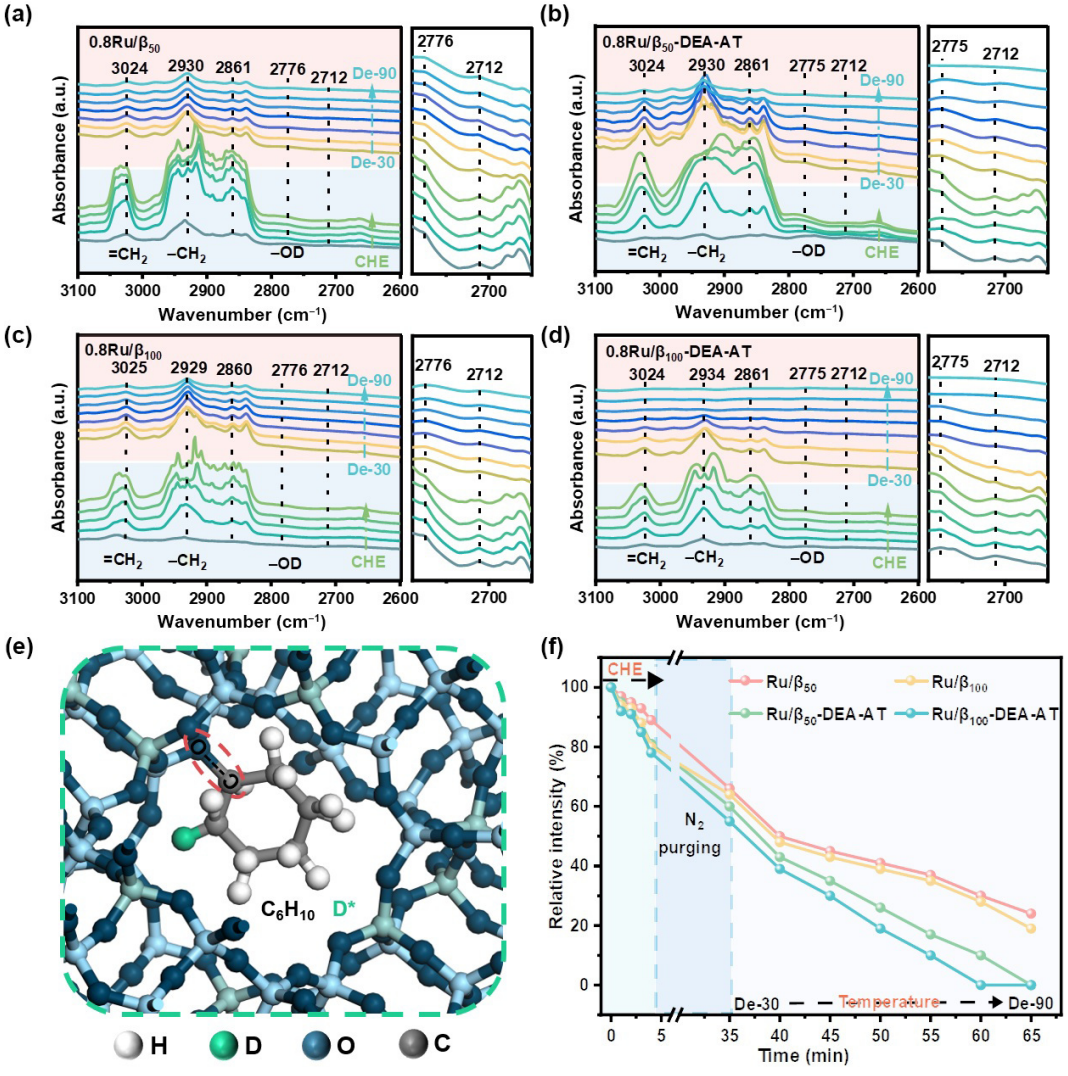

Figure 7 (a) Investigation of the protonation ability of cyclohexene. *In-situ* FTIR spectra of (a) β_{50}, (b) β_{50}-DEA-AT, (c) β_{100}, and (d) β_{100}-DEA-AT. Each scan was completed within approximately one min (light blue shaded regions in Figs. 6(a)–6(d)). Once the adsorption reached equilibrium, the CHE-containing stream was replaced with pure N_2 (50 mL·min^{-1}) for 30 min to purge physisorbed species. Thereafter, the temperature increased from 30 to 90 °C at a rate of 2 °C·min^{-1}, with spectra collected every 5 min (pink shaded regions in Figs. 6(a)–6(d)). (e) A conceptual illustration of the transformation from the –OD groups to the C–O species at the W–OH site. (f) The relative intensity changes of –OD absorption peaks (2712 cm^{-1}) over time were compared across different catalysts.

& editing. Z. H. C.: Formal analysis, writing – review & editing. W. F. L. and Y. H. J.: Formal analysis. P. Y.: Resources. X. P. M.: Resources. Y. J. Z.: Resources, formal analysis. J. J. Z.: Resources, formal analysis. L. W.: Resources, formal analysis. J. F.: Formal analysis, writing – review draft, writing, review & editing. L. H.: Formal analysis, writing, review & editing, funding acquisition. Z. K. P.: Formal analysis, writing – review & editing, funding acquisition, supervision. All the authors have approved the final manuscript.

Use of AI statement

None.

References

[1] Cheng, K.; Smulders, L. C. J.; van der Wal, L. I.; Oenema, J.; Meeldijk, J. D.; Visser, N. L.; Sunley, G.; Roberts, T.; Xu, Z. R.; Doskocil, E. et al. Maximizing noble metal utilization in solid catalysts by control of nanoparticle location. *Science* **2022**, *377*, 204–208.

[2] Zhang, X. J.; Yan, T.; Hou, H. M.; Yin, J. Q.; Wan, H. L.; Sun, X. D.; Zhang, Q.; Sun, F. F.; Wei, Y.; Dong, M. F et al. Regioselective hydroformylation of propene catalysed by rhodium-zeolite. *Nature* **2024**, *629*, 597–602.

[3] Jia, Y. H.; Li, H.; Feng, J.; Lang, W. F.; Zhang, L. Z.; Kim, Y. D.; Wang, J. T.; Liu, Z. Y.; Peng, Z. K. Enhanced benzene alkylation via cyclohexene activation regulated by grafted sulfonic groups. *Fuel* **2025**, *397*, 135414.

[4] Jia, Y. H.; Sun, K. H.; Li, J. P.; Zhang, L. Z.; Zhao, S. F.; Kim, Y. D.; Feng, J.; Li, B. J.; Liu, Z. Y.; Peng, Z. K. Synergistic metal-acid unit for boosting tandem catalysis via efficient transformation of the key intermediate. *ACS Catal.* **2025**, *15*, 21186–21201.

[5] Li, J. P.; Sun, K. H.; Huang, J. Y.; Jia, Y. H.; Zhao, S. F.; Kim, Y. D.; Han, L.; Li, B. J.; Feng, J.; Liu, Z. Y. et al. Confined metal-acid units for boosting benzene hydroalkylation via efficient activation of key intermediate. *Nano Res.* **2025**, *18*, 94907138.

[6] Cheng, L. L.; Tian, S. N.; Liang, D.; Gu, J.; Chen, R. Z.; Chen, X. R.; Yuan, H. R.; Chen, Y. Enhanced hydroconversion of polyethylene via dual-functional catalysis: Exploiting ZSM-22 pore-mouth catalysis

and Ru electronic effect. *Chem. Eng. J.* **2024**, *486*, 150332.
[7] Mu, C.; Sun, J. H.; Xie, C.; Bao, J. X.; Guo, X.; Zhang, H. Z.; Zhao, Y. J.; Wang, S. P.; Ma, X. B. Shape selectivity of AEL channels for anomalously facilitating biojet fuel production from long-chain *n*-alkane hydrocracking. *ACS Catal.* **2024**, *14*, 1394–1404.
[8] Chen, R. Z.; Cheng, L. L.; Gu, J.; Yuan, H. R.; Chen, Y. Mechanistic understanding of metal-acid synergetic hydroconversion of polyethylene under mild conditions over a Ru/MOR catalyst. *Energy Convers. Manage.* **2024**, *300*, 117983.
[9] Ge, J.; Wang, G. H.; Sui, W.; Si, C. L.; Guo, H. R.; Ni, Y. H.; Hu, J. G. Highly efficient metal-acid synergetic catalytic fractionation of lignocellulose under mild conditions over lignin-coordinated N-anchoring Co single-atom catalyst. *Chem. Eng. J.* **2023**, *462*, 142109.
[10] Feng, J.; Liu, Q. Y.; Li, H. J.; Song, Z. X.; Dong, L.; Zhao, S. F.; Kim, Y. D.; Liu, Z. Y.; Peng, Z. K. Tuning the selectivity of benzene hydroalkylation over PdZn/HBeta catalysts: Identification of lattice contraction and electronic properties. *Catal. Sci. Technol.* **2023**, *13*, 1470–1481.
[11] Song, Y. H.; Zhang, M.; Fan, G. L.; Yang, L.; Li, F. Combining a supported Ru catalyst with HBeta zeolite to construct a high-performance bifunctional catalyst for one-step cascade transformation of benzene to cyclohexylbenzene. *Ind. Eng. Chem. Res.* **2022**, *61*, 18663–18675.
[12] Zhang, Y. J.; Yang, Y. S.; Hou, Q. D.; Xu, E. Z.; Wang, L.; Li, F.; Wei, M. Metal-acid bifunctional catalysts toward tandem reaction: One-step hydroalkylation of benzene to cyclohexylbenzene. *ACS Appl. Mater. Interfaces* **2022**, *14*, 31998–32008.
[13] Zhang, M.; Fan, G. L.; Li, F. Significant promotional effect of Nb doping in bifunctional Pd/WO_x nanocatalysts on one‐step benzene hydroalkylation. *ChemCatChem* **2024**, *16*, e202400387.
[14] Qiu, J.; Komura, K.; Kubota, Y.; Sugi, Y. Synthesis of cyclohexylbenzene by hydroalkylation of benzene over Pd/Hβ binary catalyst. *Chinese. J. Catal.* **2007**, *28*, 246–250.
[15] Zhang, Y. J.; Hou, Q. D.; Wang, S.; Xu, E. Z.; Zhao, S. Q.; Li, F.; Yang, Y. S.; Wei, M. Metal-acid interface engineering in Pd–WO_x bifunctional catalysts for the hydroalkylation tandem reaction of benzene. *ACS Appl. Mater. Interfaces* **2023**, *15*, 33612–33620.
[16] Xue, C. H.; Hou, X. H.; Sun, W. J.; Yuan, X. Direct thermal reduction of Ni/Hβ and its improved catalytic performance with stability in hydroalkylation of benzene. *J. Porous. Mater.* **2025**, *32*, 341–351.
[17] Bolshakov, A.; van de Poll, R.; van Bergen-Brenkman, T.; Wiedemann, S. C. C.; Kosinov, N.; Hensen, E. J. M. Hierarchically porous FER zeolite obtained via FAU transformation for fatty acid isomerization. *Appl. Catal. B: Environ.* **2020**, *263*, 118356.
[18] Lee, S. U.; Lee, Y. J.; Kim, J. R.; Jeong, S. Y. Rational synthesis of silylated Beta zeolites and selective ring opening of 1-methylnaphthalene over the NiW-supported catalysts. *Appl. Catal. B: Environ.* **2017**, *219*, 1–9.
[19] Liu, B. Y.; Oh, S. C.; Chen, H. Y.; Liu, D. X. The effect of oxidation of ethane to oxygenates on Pt- and Zn-containing LTA zeolites with tunable selectivity. *J. Energy Chem.* **2019**, *30*, 42–48.
[20] Gao, X.; Ding, Y. Y.; Peng, L. L.; Yang, D.; Wan, X. Y.; Zhou, C. M.; Liu, W.; Dai, Y. H.; Yang, Y. H. On the effect of zeolite acid property and reaction pathway in Pd-catalyzed hydrogenation of furfural to cyclopentanone. *Fuel* **2022**, *314*, 123074.
[21] Wu, Y.; Chen, C. L.; Xiong, Z.; Xu, M.; Zhao, Y.; Dai, Y. H.; Han, Y.; Zhou, Y.; Liu, X. L.; Wang, J. Metal-acid synergistic catalysis accelerates the hydrogen borrowing amination of alcohols by confining Ru sites in Beta zeolite. *Chem. Eng. J.* **2024**, *493*, 152457.
[22] Zhang, K.; Dou, X. M.; Zhou, Z. Y.; Wang, Y.; Hou, H. M.; Meira, D. M.; Liu, L. C.; He, P. Tuning the size and spatial distribution of Pt in bifunctional Pt-zeolite catalysts for direct coupling of ethane and benzene. *Chem. Eng. J.* **2024**, *497*, 154874.
[23] Tian, S. H.; Bai, R. S.; Gao, Z. R.; Chen, Z. W.; Wang, M. L.; Tang, H. Y.; Lin, S. Y.; Xu, B. J.; Liu, X.; Yu, J. H. et al. High-efficiency hydrocracking of polyolefin plastics by controlling intimacy between Pt clusters and zeolite acid sites. *J. Am. Chem. Soc.* **2025**, *147*, 30268–30276.
[24] Berdugo-Díaz, C. E.; Manetsch, M. T.; Lee, J.; Sik Yun, Y.; Yancey, D. F.; Rozeveld, S. J.; Luo, J.; Chen, X.; Flaherty, D. W. Ester reduction on bifunctional metal-acid catalysts: Effect of metal to acid ratio. *J. Catal.* **2024**, *430*, 115346.
[25] Zhang, M.; Fan, G. L.; Yang, L.; Li, F. Cooperative effect of multi-active sites in WO_x-modified ZrO_2 supported highly dispersed Pd catalysts for promoting benzene hydroalkylation. *Chem. Eng. J.* **2023**, *473*, 145456.
[26] Liu, J. Y.; Wei, J. D.; Feng, X.; Song, M. X.; Shi, S.; Liu, S. B.; Liu, G. Z. Ni/HZSM-5 catalysts for hydrodeoxygenation of polycarbonate plastic wastes into cycloalkanes for sustainable aviation fuels. *Appl. Catal. B: Environ.* **2023**, *338*, 123050.
[27] Wang, L.; Yang, Y. S.; Shi, Y. W.; Liu, W.; Tian, Z. W.; Zhang, X.; Zheng, L. R.; Hong, S.; Wei, M. Single-atom catalysts with metal-acid synergistic effect toward hydrodeoxygenation tandem reactions. *Chem Catal.* **2023**, *3*, 100483.
[28] Cui, Y. D.; Wang, N.; Bi, G. Y.; Zhuo, H. Y.; Shang, X.; Cai, T.; Jiang, W.; Ben, H. X.; Yang, X. L.; Huang, Y. Q. Efficient one-pot cellulosic ethanol production over PdZn@silicalite-1 catalysts with metal-acid "restricted adjacency" structures. *Adv. Funct. Mater.* **2025**, *35*, 2421143.
[29] Zhu, X. C.; Gao, Y.; Chen, H. R.; Jiang, M. W.; Wang, X. Y.; Miao, C. X.; Shen, Y. F.; Ji, Y. G.; Qin, Z. X.; Wu, Z. J. et al. Constructing hierarchical zeolites with highly complete framework via controlled desilication. *Angew. Chem., Int. Ed.* **2024**, *63*, e202411446.
[30] Ates, A. Effect of alkali-treatment on the characteristics of natural zeolites with different compositions. *J. Colloid Interface Sci.* **2018**, *523*, 266–281.
[31] Ding, K.; Zhong, Z. P.; Wang, J.; Zhang, B.; Addy, M.; Ruan, R. Effects of alkali-treated hierarchical HZSM-5 zeolites on the production of aromatic hydrocarbons from catalytic fast pyrolysis of waste cardboard. *J. Anal. Appl. Pyrolysis* **2017**, *125*, 153–161.
[32] Wu, G. X.; Liu, S. Y.; Chen, Z. Q.; Yu, Q. Y.; Chu, Y. H.; Xiao, H.; Peng, H.; Fang, D. X.; Deng, S. H.; Chen, Y. Q. Promotion effect of alkaline leaching on the catalytic performance over Cu/Fe-SSZ-13 catalyst for selective catalytic reduction of NO_x with NH_3. *J. Taiwan Inst. Chem. Eng.* **2022**, *134*, 104355.
[33] Wu, L.; Xin, J. J.; Xia, D.; Sun, J. L.; Liang, J. Enhanced production of hydrocarbons from the catalytic pyrolysis of maize straw over hierarchical ZSM-11 zeolites. *Appl. Catal. B: Environ.* **2022**, *317*, 121775.
[34] Gutierrez-Acebo, E.; Leroux, C.; Chizallet, C.; Schuurman, Y.; Bouchy, C. Metal/acid bifunctional catalysis and intimacy criterion for ethylcyclohexane hydroconversion: When proximity does not matter. *ACS Catal.* **2018**, *8*, 6035–6046.
[35] Vance, B. C.; Kots, P. A.; Wang, C.; Hinton, Z. R.; Quinn, C. M.; Epps, T. H.; Korley, L. T. J.; Vlachos, D. G. Single pot catalyst strategy to branched products via adhesive isomerization and hydrocracking of polyethylene over platinum tungstated zirconia. *Appl. Catal. B: Environ.* **2021**, *299*, 120483.
[36] Korpelin, V.; Sahoo, G.; Ikonen, R.; Honkala, K. ReO_x as a Brønsted acidic modifier in glycerol hydrodeoxygenation: Computational insight into the balance between acid and metal catalysis. *J. Catal.* **2023**, *422*, 12–23.
[37] Cui, X. Y.; He, H. R.; Xie, D.; Zheng, L. X.; Wang, X. B.; Jiang, Z.; Xu, D. H.; Guo, Y. Mechanism of sulfur poisoning to Ru-based catalysts in supercritical water gasification of glycerol: From experiment to combined DFT and kinetics studies. *Chem. Eng. J.* **2023**, *464*, 142622.
[38] Xie, X. W.; Li, Y.; Liu, Z. Q.; Haruta, M.; Shen, W. J. Low-temperature oxidation of CO catalysed by Co_3O_4 nanorods. *Nature* **2009**, *458*, 746–749.

[39] Liu, Y.; Liu, Q. Y.; Sun, K. H.; Zhao, S. F.; Kim, Y. D.; Yang, Y. P.; Liu, Z. Y.; Peng, Z. K. Identification of the encapsulation effect of heteropolyacid in the Si–Al framework toward benzene alkylation. *ACS Catal.* **2022**, *12*, 4765–4776.

[40] Han, X. L.; Zhou, Y. C.; Chen, S. M.; Chen, H. H.; Zhang, J. X.; Qu, Z. Y.; Zeng, F.; Ji, T.; Jiang, H.; Cao, W. et al. Hydrogen spillover-induced Brønsted acidity enables controllable hydrocracking of polyolefin waste to liquid fuels. *Angew. Chem., Int. Ed.* **2025**, *64*, e202505518.

[41] Ivanova, I. I.; Kolyagin, Y. G.; Kasyanov, I. A.; Yakimov, A. V.; Bok, T. O.; Zarubin, D. N. Time-resolved *in situ* MAS NMR monitoring of the nucleation and growth of zeolite BEA catalysts under hydrothermal conditions. *Angew. Chem., Int. Ed.* **2017**, *56*, 15344–15347.

[42] Fan, K.; Liu, S.; Wu, Q. M.; Iemhoff, A.; Kunkes, E.; De Baerdemaeker, T.; Parvulescu, A. N.; Bottke, N.; Yokoi, T.; De Vos, D. E. et al. Regulation of Al distribution in ITR zeolite for methanol to propylene. *J. Energy Chem.* **2025**, *102*, 120–125.

[43] Xiao, P. P.; Wang, Y.; Tang, X. M.; Zheng, A. M.; Baerdemaeker, T. D.; Parvulescu, A. N.; De Vos, D.; Meng, X. J.; Xiao, F. S.; Gies, H. et al. Isomers of organic structure directing agent influence the Al distribution of AEI zeolite and catalytic performance in methane oxidation. *Chin. J. Catal.* **2025**, *73*, 252–260.

[44] Groen, J. C.; Zhu, W. D.; Brouwer, S.; Huynink, S. J.; Kapteijn, F.; Moulijn, J. A.; Pérez-Ramírez, J. Direct demonstration of enhanced diffusion in mesoporous ZSM-5 zeolite obtained via controlled desilication. *J. Am. Chem. Soc.* **2007**, *129*, 355–360.

[45] Sun, M. H.; Gao, S. S.; Hu, Z. Y.; Barakat, T.; Liu, Z.; Yu, S.; Lyu, J. M.; Li, Y.; Xu, S. T.; Chen, L. H. et al. Boosting molecular diffusion following the generalized Murray's Law by constructing hierarchical zeolites for maximized catalytic activity. *Natl. Sci. Rev.* **2022**, *9*, nwac236.

[46] Hao, J. Q.; Zhou, J.; Wang, Y. D.; Li, L. Y.; Sheng, Z. Z.; Teng, J. W.; Xie, Z. K. Pore mouth catalysis promoting n-hexane hydroisomerization over a Pt/ZSM-5 bifunctional catalyst. *Chem Catal.* **2024**, *4*, 101041.

[47] Guo, C. M.; Sun, M. H.; Liu, Z.; Jiang, A. K.; Ye, B.; Xu, C.; Yang, X. Y.; Sun, B. L.; Jiang, Y.; Wu, W. et al. Hierarchical molecular highway architectures in SAPO-34 single crystals boost methanol-to-olefins catalytic performance. *ACS Catal.* **2025**, *15*, 20308–20319.

[48] Ben David, R.; Ben Yaacov, A.; Eren, B. Hydrogen exchange through hydrogen bonding between methanol and water in the adsorbed state on Cu(111). *J. Phys. Chem. Lett.* **2023**, *14*, 2644–2650.

[49] Hou, Z. Q.; Dai, L. Y.; Liu, Y. X.; Deng, J. G.; Jing, L.; Pei, W. B.; Gao, R. Y.; Feng, Y.; Dai, H. X. Highly efficient and enhanced sulfur resistance supported bimetallic single-atom palladium-cobalt catalysts for benzene oxidation. *Appl. Catal. B: Environ.* **2021**, *285*, 119844.